

Article

Pulsed Current Effect on the Hard Anodizing of an AlSi10Mg Aluminum Alloy Obtained via Additive Manufacturing

Elisa Dallari ¹, Massimiliano Bononi ¹, Annalisa Pola ², Marialaura Tocci ², Paolo Veronesi ¹ and Roberto Giovanardi ^{1,*}

¹ Department of Engineering “Enzo Ferrari”, University of Modena and Reggio Emilia, 41125 Modena, Italy

² Department of Mechanical Industrial Engineering, University of Brescia, 25123 Brescia, Italy

* Correspondence: roberto.giovanardi@unimore.it

Abstract: The hard anodizing treatments of cast Al-Si alloys are notoriously difficult. Indeed, their microstructural features hinder the growth of a uniform, compact, and defect-free anodic oxide. In this paper, AlSi10Mg samples, produced via Gravity Casting (GC) and Additive Manufacturing, i.e., Laser Powder Bed Fusion (L-PBF), were hard anodized in a sulfuric acid bath, in order to verify how the particular microstructure obtained via L-PBF affects the thickness, hardness, compactness, and defectiveness of the anodic oxide. Moreover, for the first time, Pulsed Direct Current (PDC) procedures were used to perform the hard anodizing treatments on additively manufactured AlSi10Mg alloy. Several combinations of temperature and electrical parameters, i.e., current density, frequency, and Duty Cycle, were tested. The anodized samples were characterized through optical microscopy analysis, Scanning Electron Microscopy (SEM) analysis, and accelerated corrosion tests, i.e., Potentiodynamic Polarization (POL) and Electrochemical Impedance Spectroscopy (EIS) measurements. The PDC procedures allowed improvement of the compromise between evenness, compactness, and defectiveness. Among the attempted PDC procedures, a specific combination of electrical parameters and temperature allowed the best results to be obtained, i.e., the highest hardness and the lowest volumetric expansion values without compromising the oxide quality rating and the corrosion resistance behavior. However, none of the attempted PCD strategies allowed the hardness values obtained on samples produced via GC to be reached.



Citation: Dallari, E.; Bononi, M.; Pola, A.; Tocci, M.; Veronesi, P.; Giovanardi, R. Pulsed Current Effect on the Hard Anodizing of an AlSi10Mg Aluminum Alloy Obtained via Additive Manufacturing. *Surfaces* **2023**, *6*, 97–113. <https://doi.org/10.3390/surfaces6010008>

Academic Editor: Gaetano Granozzi

Received: 23 February 2023

Revised: 6 March 2023

Accepted: 10 March 2023

Published: 13 March 2023



Copyright: © 2023 by the authors. Licensee MDPI, Basel, Switzerland. This article is an open access article distributed under the terms and conditions of the Creative Commons Attribution (CC BY) license (<https://creativecommons.org/licenses/by/4.0/>).

Keywords: anodizing; AlSi10Mg; L-PBF; pulsed current

1. Introduction

Conventional anodizing of Al alloys is generally carried out in order to increase the corrosion resistance of the parts, especially when exposed to aggressive environments, and/or their aesthetic quality [1]. While wrought Al-Si-Mg alloys are particularly suitable for anodization, the anodizing of casting Al-Si alloys is usually difficult because of the microstructural features of these materials. In fact, the presence of secondary and eutectic phases that surround Al dendrites represent an obstacle to the growth of a uniform and compact oxide layer with a low level of defects [2–4]. Specifically, the significant Si content of these alloys is a critical aspect because Si particles are anodized at a lower rate than the Al matrix. Therefore, during anodizing, the Si particles are not completely oxidized, but only an extremely thin oxide film (in the order of tens of nanometers) is formed on Si particles, while the rest of the particle is embedded in the oxide layer developing on the surface of the component [4,5]. Furthermore, the presence of Si particles is responsible for the formation of porosities and cracks in the oxide film [6]. Some studies reported that the morphology and distribution of secondary phases influence the quality of the anodized layer, according also to the manufacturing process [7,8]. Small and fibrous Si particles (such as those obtained after eutectic modification by Sr addition) are less detrimental than

coarse and flake-like particles [3]. In addition, uniform distribution of these particles is positive in terms of the uniform thickness of the oxide layer [3,8].

Lately, Al alloys such as AlSi12, AlSi10Mg, and AlSi7Mg have been used for the production of components using Additive Manufacturing (AM) technologies. One of the peculiarities of this process consists of extremely high thermal gradients and cooling rate when the material is melted using a laser as a concentrated source of energy, followed by the material solidifying [9,10]. This results in an extremely fine microstructure, with Al cells with a size in the order of tens of microns surrounded by a network of Si particles. When compared to the cast counterpart with the same chemical composition, samples produced using AM exhibit a much finer microstructure with a more homogeneous distribution of secondary phases, together with higher hardness and strength due to several combined strengthening mechanisms [11]. Therefore, it appears reasonable to expect a different anodizing behavior for these materials in comparison with the counterpart cast alloys.

Revilla et al. [12–15] investigated the anodizing behavior of Al-Si alloys produced by the Laser Powder Bed Fusion (L-PBF) process. In a study on AlSi10Mg alloy, it was concluded that Si particles were completely oxidized due to their extremely fine size when compared with cast alloy with the same chemical composition [14]. This resulted in the consumption of a large fraction of the anodic charge during anodization and, therefore, the growth rate of the anodic layer was significantly lower for the L-PBF samples than for the cast alloy [15]. This led to an overall lower thickness of the oxide film, even though it was uniform in thickness and smoothness [14,15]. In addition, branched-like pores formed, uniformly distributed in the oxide layer. Therefore, a general poor efficiency of the anodizing process was deduced for L-PBF Al-Si alloys. Moreover, the coarser microstructural features along the melt pool boundary resulted in a slightly thinner oxide layer in such positions [14], while the different size of Al cells on surfaces normal or parallel to the building direction was responsible for an anisotropic behavior during anodizing. On the other hand, no significant differences in oxide growth rate were observed during anodization of L-PBF Al-Si alloys, with Si content ranging from 7 to 12 wt% [13]. The presence of porosities in the alloy is also a critical issue for the anodizing behavior because it was observed that small cracks form in the oxide layer at the side of pre-existing pores [13]. This is likely due to the different volumetric expansion of the material in these areas during the treatment. The heat treatment of L-PBF Al-Si alloys can significantly affect the properties of the oxide layer according to the microstructural changes that take place in the material. In fact, if during heat treatment the network of Si particles is broken up, the resulting coarser and disconnected Si particles are not completely oxidized during anodizing, as happens for cast alloys.

Hard anodizing is an alternative surface treatment that is able to produce a thicker (thickness of 50–100 μm vs. 5–20 μm [1] of conventional anodizing) and harder oxide layer, which is beneficial for enhancing surface hardness and wear resistance, besides providing a positive effect also on corrosion resistance. Hard anodizing has been applied on both wrought [16–18] and casting [5,19,20] alloys. Nevertheless, the formation of a thick, compact, and uniform oxide layer is hindered by the same problems related to the presence of the secondary phases discussed above for conventional anodizing. In order to overcome this limitation, anodizing applying a pulsed current can represent an interesting alternative to investigate. In fact, some studies [21–23] pointed out that the application of pulsed current was positive for the anodizing of wrought Al alloys containing several secondary phases. Specifically, this application of the current avoids electrical field concentration on the secondary phases, hindering the parasitic reactions that create micro-voids and microcracks and bringing a more homogeneous growth of the oxide layer, even in the presence of abundant secondary phases. Recently, pulsed anodizing was also used to successfully increase the wear resistance of a hypereutectic Al cast alloy [24]. Therefore, in the present study, hard anodization of AlSi10Mg alloy was carried out by means of direct and pulsed current in order to investigate the material response in terms of the quality of the external oxide (i.e., the presence of defects, hardness, and volumetric expansion ratio)

and corrosion resistance. The alloy was tested under the L-PBF as-built condition to verify how the very fine microstructure and particular Si distribution described above affect the quality of the oxide and how the pulsed current parameters can further improve the results obtained, even in terms of hardness and thickness. For comparison, samples with the same chemical composition but produced by the conventional Gravity Casting (GC) foundry process were anodized and tested, applying the same experimental conditions.

2. Materials and Methods

A series of rod-shaped specimens of AlSi10Mg aluminum alloy were fabricated by GC and L-PBF. The GC rod-shaped specimens were cast in a steel permanent mold after modification treatment. The L-PBF rod-shaped specimens were produced using an EOS M 290 metal 3D printer. The powder used for sample production was the commercial EOS Aluminum AlSi10Mg. The chosen processing parameters were 400 W of laser power, 100 μm of focus diameter, and 30 μm of layer thickness [25]; the L-PBF rod-shaped specimens were built in the vertical direction. The rod-shaped specimens, marked by a diameter of 16 mm, were sliced into disc-shaped samples with a thickness of 2.5 mm. The hard anodizing treatments were carried out on the as-produced disc-shaped samples.

2.1. Hard Anodizing Treatments

The hard anodizing treatments were performed in a laboratory pilot plant already adopted in the previous works of the authors [17,21–23,26]. The laboratory pilot plant consists of an AMEL Instrument 568 galvanostat/potentiostat connected to a programmable function generator and equipped with fourteen supplementary batteries Nickel-Metal Hydride 8.4 V, a Keithley 2000 ammeter, a voltmeter, a voltage divider linked with a computer synchronized PicoScope 2000 data-logger, and an electrochemical anodizing cell. The electrochemical anodizing cell is made up of a cooling system connected to a Julabo F32 refrigerated circulator, an insufflating air system, a thermometer, an electrolyte solution, a 6060 aluminum alloy cathode, and a sample holder. The sample holder ensures that the sample-exposed area remains constant and equal to 1 cm^2 .

The electrolyte solutions, defined to simulate a real industrial anodizing bath (so containing Al^{3+} ions that comes from the anodizing process itself), have a concentration of sulfuric acid H_2SO_4 equal to 190 g/L, a concentration of aluminum ions Al^{3+} equal to 8 g/L, and a temperature ranging from 0 $^\circ\text{C}$ to 7 $^\circ\text{C}$. The aforementioned values of concentration and temperature were selected in accordance with the optimization studies carried out in the previous works of the authors [17,21,26].

Before the hard anodizing treatment, each sample was polished with silicon carbide grinding paper, FEPA P #1200/US #500 (grain size 15 μm), cleaned with acetone, and rinsed with distilled water.

In order to study the effect of the electrical cycle, two distinct procedures were performed. The first one was in Direct Current (DC) and the second one was in Pulsed Direct Current (PDC). The DC procedures were performed on GC and L-PBF samples. Instead, the PDC procedures were carried out only on L-PBF samples. For the purpose of ensuring correspondence between the different experimental data, a common theoretical value of the exchanged charge (Q) of 100 C was fixed. The chosen value of Q allows a coating of 45–65 μm , largely employed in industrial practice, to be obtained.

2.1.1. Direct Current (DC) Procedures

The DC procedures employed an electrical cycle divided into two segments. The first one was a current ramp characterized by a constant inclination value equal to 0.1 $\text{mA}/\text{cm}^2\text{s}$, whereas the second one was a galvanostatic plateau with a constant current density value.

As can be seen in Table 1, the electrolyte solution temperature was set at 0 °C; meanwhile, two constant current density values were tested: 25 and 40 mA/cm².

Table 1. Schematization of electrolyte solution conditions and electrical parameters adopted in Direct Current (DC) procedures.

Sample	Solution Conditions				Electrical Parameters				
	H ₂ SO ₄ (g/L)	Al ³⁺ (g/L)	T (°C)	Charge (C)	Constant Current Density (mA/cm ²)	Initial Ramp Inclination (mA/cm ² s)	Initial Ramp Duration (s)	Constant Value Duration (s)	Total Duration (s)
GC0—25	190	8	0	100	25	0.1	250	3875	4125
GC0—40	190	8	0	100	40	0.1	400	2300	2700
L-PBF0—25	190	8	0	100	25	0.1	250	3875	4125
L-PBF0—40	190	8	0	100	40	0.1	400	2300	2700

2.1.2. Pulsed Direct Current (PDC) Procedures

The PDC procedures utilized a rectangular-shaped electrical waveform consisting of instantaneous transitions between two current density levels: peak current density (I_{on}) and background current density (I_{off}).

Regardless of the PDC procedure carried out, the background current density value was set at 6 mA/cm². As can be seen in Table 2, a first fixed value of Duty Cycle (DC%) was adopted (25%), changing the other parameters as follow: two values of electrolyte solution temperature (0–7 °C), two values of average current density (25–40 mA/cm²), and two values of frequency (0.05–50 Hz); the tested current densities (25 and 40 mA/cm²) fall within the range of average current density commonly used in the literature [17,21–23,26–31]. Afterward, four different values of DC% (12.5, 50, 75, 90%) were tested with fixed values of electrolyte solution temperature, average current density, and frequency, i.e., 0 °C, 25 mA/cm², and 50 Hz, respectively.

Table 2. Schematization of electrolyte solution conditions and electrical parameters adopted in Pulsed Direct Current (PDC) procedures.

Sample	Solution Conditions				Electrical Parameters							
	H ₂ SO ₄ (g/L)	Al ³⁺ (g/L)	T (°C)	Charge (C)	Average Current Density (mA/cm ²)	Frequency (Hz)	DC% (%)	I _{on} (mA/cm ²)	t _{on} (s)	I _{off} (mA/cm ²)	t _{off} (s)	Total Duration (s)
82—6, 0.05 Hz, 0 °C	190	8	0	100	25	0.05	25	82	5	6	15	4000
82—6, 0.05 Hz, 7 °C	190	8	7	100	25	0.05	25	82	5	6	15	4000
82—6, 50 Hz, 0 °C	190	8	0	100	25	50	25	82	0.005	6	0.015	4000
82—6, 50 Hz, 7 °C	190	8	7	100	25	50	25	82	0.005	6	0.015	4000
142—6, 0.05 Hz, 0 °C	190	8	0	100	40	0.05	25	142	5	6	15	2500
142—6, 0.05 Hz, 7 °C	190	8	7	100	40	0.05	25	142	5	6	15	2500
142—6, 50 Hz, 0 °C	190	8	0	100	40	50	25	142	0.005	6	0.015	2500
142—6, 50 Hz, 7 °C	190	8	7	100	40	50	25	142	0.005	6	0.015	2500
158—6, 50 Hz, 0 °C, DC 12.5%	190	8	0	100	25	50	12.5	158	0.0025	6	0.0175	4000
44—6, 50 Hz, 0 °C, DC 50%	190	8	0	100	25	50	50	44	0.01	6	0.01	4000
31.3—6, 50 Hz, 0 °C, DC 75%	190	8	0	100	25	50	75	31.3	0.015	6	0.005	4000
27.1—6, 50 Hz, 0 °C, DC 90%	190	8	0	100	25	50	90	27.1	0.018	6	0.002	4000

2.2. Characterization Techniques

The obtained anodic oxides were characterized through spectrophotometry analysis, optical microscopy analysis, scanning electron microscopy analysis, and accelerated corrosion tests.

The spectrophotometry analysis, carried out with an X-rite series SP60 spectrophotometer, acquires the brightness parameter (L^*) of three-dimensional CIELAB color space. The L^* values were calculated as the average of three measurements. Each measurement was performed two hours after the end of the hard anodizing treatment in order to enable the natural sealing of the porous structure of the anodic oxide.

The optical microscopy analysis, performed with a Leica DMI5000 M inverted microscope, allowed determination of the following parameters:

- Microstructure of both GC and L-PBF bare samples. AM samples were observed after Keller etching (1% HF, 1.5% HCl, 2.5% HNO₃ and 95% H₂O) for 30 s according to ASTM E407 standard.
- Anodic oxide thickness. For each sample, the anodic oxide thickness value was calculated as an average of ten measurements acquired in five different cross-section micrographs at 100× magnification.
- Volumetric expansion ratio, V_{ox}/V_{Al} . The V_{ox}/V_{Al} values were calculated according to previous works [26,32,33] based on measuring the aluminum converted thicknesses and the anodic oxide thicknesses. In order to do this, in each sample two different cross-section micrographs at 100× magnification were acquired; a high value of the volumetric expansion ratio suggests a poor anodic oxide density due to a large distribution of defects and porosity.
- Faradaic efficiency, η . The η values, defined as a ratio between the effective converted mass ($m_{eff.}$) and the theoretical converted mass ($m_{theor.}$), were calculated as in previous work [26]. The $m_{eff.}$ values were determined by setting 1.0 cm² as the exposed area and 2.67 or 2.68 g/cm³ as the density for GC and L-PBF samples, respectively [25]. The $m_{theor.}$ value was determined using Faraday's law [34] by setting 27.1652 g/mol as the molar mass, 100 C as the total charge transferred, 2.7031 as the number of electrons exchanged, and 96,485 C/mol as the Faraday constant.
- Vickers hardness, HV_{0.025}. For each sample, the HV_{0.025} value was calculated as an average of fifteen measurements carried out with a Wolpert Wilson® Instruments 402 MVD Microhardness Tester using 25 gf as test load and 10 s as dwell time. To this end, in each sample five different cross-section micrographs at 200× magnification were acquired.

The scanning electron microscopy analysis, carried out with a Philips XL30 Environmental Scanning Electron Microscope (ESEM), permitted the evaluation of the oxide quality rating, ranging from 0 to 10. For each sample, the oxide quality rating was determined by counting the number of critical defects at the metal/oxide interface [17]. Specifically, values of 0 and 10 correspond to anodic oxides in poor and excellent conditions, respectively. In order to do this, two cross-section micrographs at 100× magnification and two cross-section micrographs at 1000× magnification were acquired.

The accelerated corrosion tests were performed according to ASTM Standards G3 and G5 [35,36], using a K0235 Flat Cell connected to a VersaSTAT 3 galvanostat/potentiostat. In the K0235 Flat Cell, the Working Electrode (WE), the Reference Electrode (RE), and the Counter Electrode (CE) were a Silver–Silver Chloride Electrode (SSCE—Ag/AgCl/KCl_{sat}) and a platinum grid, respectively. A 3.5 wt% NaCl aqueous solution was used as the electrolyte. In order to ensure a high level of comparability, all accelerated corrosion tests were performed five days after the hard anodizing treatments. Before starting each Electrochemical Impedance Spectroscopy (EIS) and Potentiodynamic Polarization (POL) test, the sample was immersed in the 3.5 wt% NaCl solution for 300 s to reach a stable value of the Open Circuit Potential (OCP). In the EIS measurements, the frequency varied from 100 kHz to 10 mHz, and the applied amplitude was 10 mV RMS. The resulting Nyquist plots were interpolated through R(QR) and R(QR)(QR)(QR) equivalent electrical circuits using ZSimpWin® EIS data analysis software. An R(QR) circuit was employed for the “L-PBF BARE” specimen, and an R(QR)(QR)(QR) circuit was employed for the remaining L-PBF samples. The POL measurements were performed from 0 V (vs. OCP) to −0.4 V (vs. OCP) and, afterward, from −0.4 V (vs. OCP) to +1.6 V (vs. OCP), with a scan rate

of 0.5 mV/s. On the resulting $E-\text{Log}_{10}(i)$ curves, Tafel analysis was applied to calculate corrosion current density (i_{corr}) and corrosion potential (E_{corr}).

3. Results and Discussion

The as-produced GC samples exhibit the typical Al-rich dendritic structure surrounded by the modified eutectic, Figure 1a. A magnification of the eutectic Si particles is visible in Figure 1b. Figure 1c shows the microstructure of the L-PBF samples characterized along the vertical cross section by semicircular melt pools due to the manufacturing process. At higher magnification, it is possible to appreciate the fine continuous network of eutectic Si (black) surrounding Al cells (white), as also reported in the literature, Figure 1d [25].

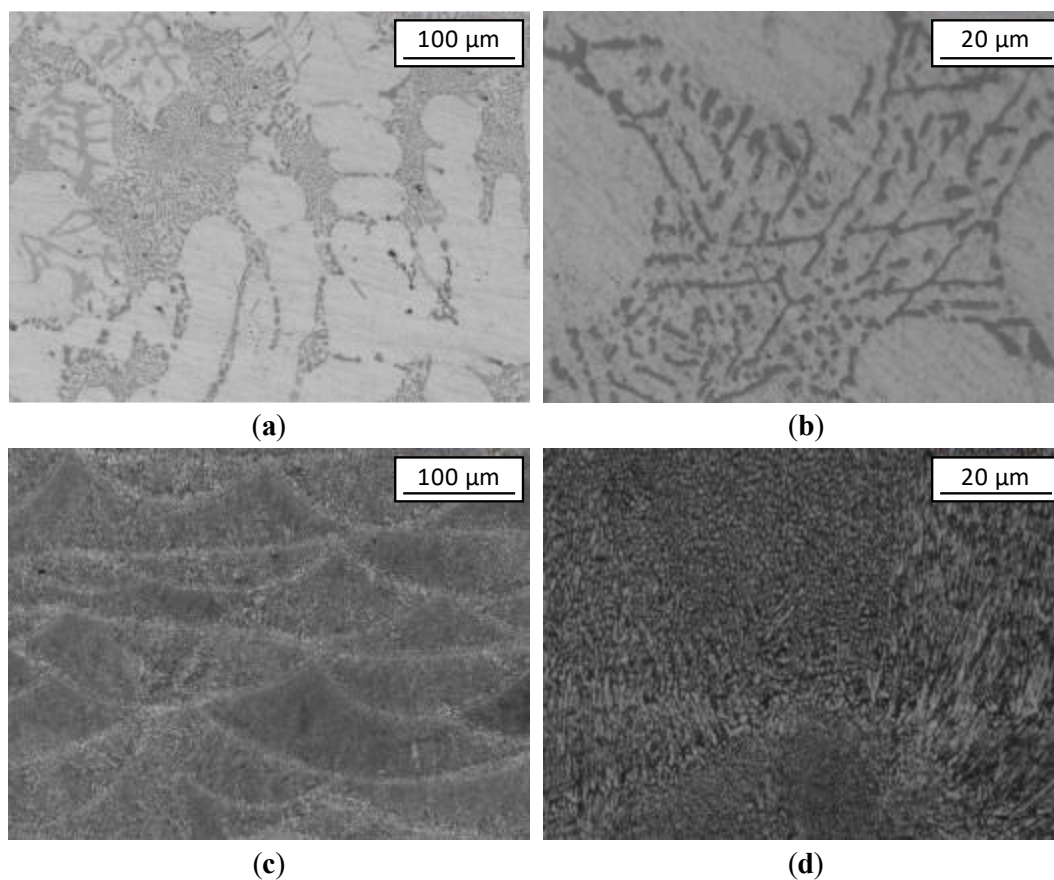


Figure 1. Micrographs of AlSi10Mg alloy produced using (a,b) GC and (c,d) L-PBF processes.

One initial important difference between the behavior of GC and L-PBF samples was observed during the anodizing process: the E vs. t potential curves acquired using DC anodizing procedures (not reported in the paper) show a sudden growth in L-PBF samples. This gives an indication of the higher compactness in L-PBF samples' anodic oxides compared to GC ones. In fact, as the compactness increases, the resistance to electrical current flow increases.

Table 3 shows the results obtained by spectrophotometry, optical microscopy, and scanning electron microscopy analyses on all the anodized samples realized.

Table 3. Results obtained by spectrophotometry, optical microscopy, and scanning electron microscopy analyses.

Sample	HV _{0.025}	Oxide Quality Rating	L*	Oxide Thickness	V _{ox} /V _{Al}	η
	(—)	(—)	(—)	(μm)	(—)	(%)
GC0—25	387.68 ± 67.62	3.5	39.71 ± 0.15	58.04 ± 30.74	1.87 ± 0.05	100
GC0—40	378.26 ± 35.08	4.0	39.52 ± 0.09	64.67 ± 21.52	2.22 ± 0.50	100
L-PBF0—25	264.20 ± 24.29	8.0	39.49 ± 0.15	54.43 ± 13.55	2.19 ± 0.17	83
L-PBF0—40	267.00 ± 44.69	7.5	40.48 ± 0.06	56.04 ± 7.51	2.12 ± 0.17	81
82—6, 0.05 Hz, 0 °C	230.31 ± 24.46	7.0	47.52 ± 0.09	61.67 ± 16.03	2.13 ± 0.44	79
82—6, 0.05 Hz, 7 °C	246.95 ± 63.79	7.5	44.27 ± 0.16	52.27 ± 13.06	1.63 ± 0.33	85
82—6, 50 Hz, 0 °C	261.01 ± 50.18	5.0	37.01 ± 0.19	45.75 ± 13.63	2.24 ± 0.75	50
82—6, 50 Hz, 7 °C	238.45 ± 67.25	5.5	35.68 ± 0.45	51.58 ± 16.48	1.96 ± 0.49	73
142—6, 0.05 Hz, 0 °C	191.72 ± 64.96	6.5	47.13 ± 0.11	62.48 ± 11.51	2.14 ± 0.03	71
142—6, 0.05 Hz, 7 °C	198.00 ± 63.16	7.0	44.65 ± 0.09	55.14 ± 15.27	1.85 ± 0.10	83
142—6, 50 Hz, 0 °C	238.93 ± 68.58	6.0	37.80 ± 0.01	56.77 ± 18.92	2.24 ± 0.34	51
142—6, 50 Hz, 7 °C	207.40 ± 66.45	6.0	36.83 ± 0.27	51.25 ± 17.68	2.05 ± 0.09	68
158—6, 50 Hz, 0 °C, DC 12.5%	225.91 ± 58.32	5.5	35.41 ± 0.26	54.95 ± 24.92	2.26 ± 0.83	57
44—6, 50 Hz, 0 °C, DC 50%	255.99 ± 41.55	6.0	37.65 ± 0.26	49.95 ± 14.97	2.01 ± 0.22	59
31.3—6, 50 Hz, 0 °C, DC 75%	267.20 ± 46.59	7.0	36.42 ± 0.28	55.15 ± 12.15	2.33 ± 0.60	68
27.1—6, 50 Hz, 0 °C, DC 90%	279.70 ± 88.86	7.5	35.72 ± 0.22	49.39 ± 14.49	1.55 ± 0.28	71

The standard deviation values of thickness in the “GC0—25” and “GC0—40” specimens reveal the presence of inhomogeneous anodic oxide layers. Compared to the “GC0—25” and “GC0—40”, the “L-PBF0—25” and “L-PBF0—40” specimens are characterized by lower Vickers hardness values due to the incorporation of the soft secondary Si-rich phases in L-PBF sample anodic oxides.

It should be specified that the HV_{0.025} measurements on the GC samples were performed far from defects, Figure 2a. On the other hand, the “L-PBF0—25” and “L-PBF0—40” specimens are marked by higher oxide quality ratings, as can be observed also in Figure 2b; the little micro-voids visible on the cross-section of Figure 2b can be related to very fine and soft silicon particles incorporated in the oxide during anodizing and removed during the polishing of the sample; EDS microanalysis of the oxide of Figure 2b allows the following composition of the coating (in weight) to be obtained: Al 43%, O 50%, Si% 7 (a small trace of sulfur deriving from the sulphate ions of the anodizing bath was removed in order to perform the quantitative analysis), values that confirm the incorporation of silicon in the oxide, as soft micro-particles (EDS microanalysis can detect the presence of silicon particles under the surface, acquiring a signal from almost 1 micron of depth). The presence of coarse secondary Si-rich precipitates in the GC samples causes the formation of punctual defects such as conical asperities. Instead, the presence of fine silicon phases in the L-PBF samples, although affecting the hardness of the oxide, avoids the formation of critical defects. Finally, the “L-PBF0—25” and “L-PBF0—40” specimens are characterized by lower faradaic efficiency values than the “GC0—25” and “GC0—40” ones. This can be explained by the partial oxidation of silicon in L-PBF samples in conflict with the η calculation hypothesis, i.e., the non-oxidation of silicon. Indeed, changing the number of exchanged silicon electrons from 0 to 4 would determine an increase in the faradaic efficiency values.

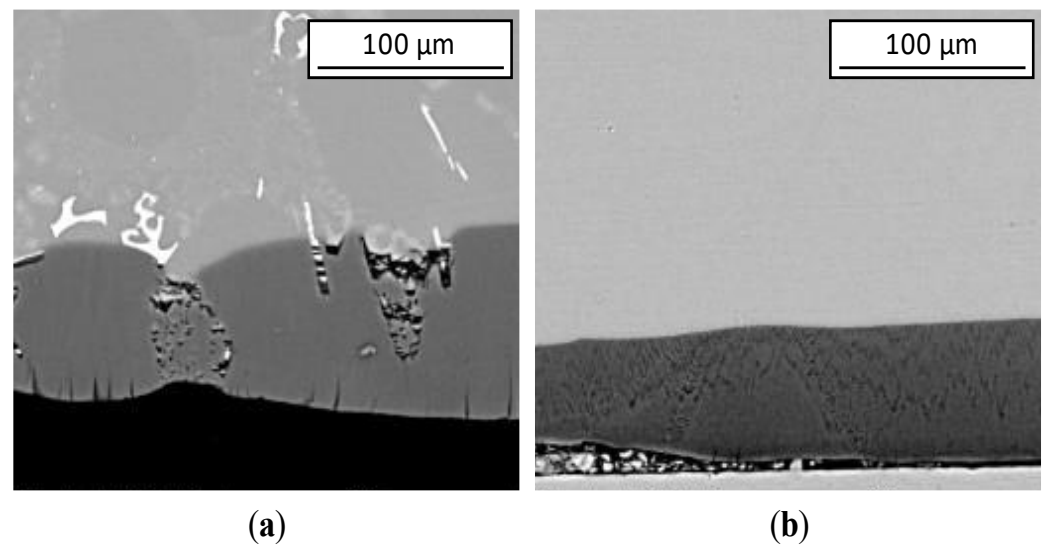


Figure 2. Examples of cross-section micrographs acquired through the Philips XL30 ESEM using a solid-state BSE detector, 30.0 kV of high voltage, 1000× of magnification, 3.5 of spot size, and 11.0 mm of working distance for (a) “GC0—25” and (b) “L-PBF0—25” specimens.

In relation to DC procedures, PDC procedures using a constant Duty Cycle establish a drop in $HV_{0.025}$ values. Among the PDC procedures using a constant Duty Cycle (25%), the “82—6, 50 Hz, 0 °C” procedure allows the highest $HV_{0.025}$ value to be obtained. On the other hand, the above-mentioned procedure is characterized by a low oxide quality rating, a high V_{ox}/V_{Al} value, and a low η value. The oxide quality rating, being equal to 5.0, is sufficient to exclude the detachment of anodic oxide fragments. The high V_{ox}/V_{Al} value reveals low compactness, which means there is a large distribution of defects and porosity. The low η value indicates a complete oxidation of silicon or, alternatively, a current dissipation due to the development of undesired parasitic reactions, e.g., oxygen evolution. The oxygen evolution parasitic reaction causes the growth of a porous and highly flawed anodic oxide layer. In this case (“82—6, 50 Hz, 0 °C” procedure) the high hardness obtained can be ascribed to an almost-complete silicon oxidation, but in the presence of important microstructural defects. The presence of oxidized silicon is also supported by EDS microanalysis in the oxide cross-section, that for the “82—6, 50 Hz, 0 °C” sample detects one of the highest percentages of silicon in the oxide (close to 14% by weight), confirming the fact that the silicon is not partially lost during the preparation of the sample (i.e., it is not present as a soft silicon secondary phases that can be easily removed during polishing, but it is oxidized and incorporated into the aluminum oxide during its growth).

Testing various Duty Cycle values allows the discovery of a PDC procedure capable of obtaining an L-PBF sample anodic oxide with the highest $HV_{0.025}$ value and the lowest V_{ox}/V_{Al} value on record. In fact, the above-mentioned PDC procedure, i.e., “27.1—6, 50 Hz, 0 °C, DC 90%”, produces an anodic oxide layer with values of Vickers hardness, oxide quality rating, volumetric expansion ratio, and faradaic efficiency equal to 279.70, 7.5, 1.55, and 71%, respectively. This value of V_{ox}/V_{Al} , compared with the Pilling–Bedworth Ratio for Al with Al_2O_3 , i.e., 1.29 [37], suggests the presence of a coating characterized by a high density due to an extremely limited distribution of defects and porosity. This means that, as suggested by the high η value, fewer undesired parasitic reactions have taken place. In this case (“27.1—6, 50 Hz, 0 °C, DC 90%” procedure) the high hardness obtained can be ascribed to a compact microstructure (without defects and with limited porosity), but in the presence of a limited silicon oxidation.

It should be noted that as the Duty Cycle increases, the Vickers hardness values, oxide quality ratings, and faradaic efficiency values increase and the volumetric expansion ratio values decrease, Figure 3. This means that increasing the DC% (and for our experiments, performed with a fixed charge exchanged, this also means decreasing the I_{on} value) the

microstructural quality of the oxide increases (limited porosity, no defects); in addition, the amount of oxidized silicon decreases. Unfortunately, none of the electrical parameter combinations applied allowed the two effects that lead to an increase in hardness to be simultaneously obtained (i.e., increase in microstructural quality and increase in the amount of oxidized silicon). Specifically, it seems that, in order to obtain the best result in terms of oxide quality, it is important to apply low current levels (I_{on}) for a long time (high DC%), conditions that do not allow silicon oxidation.

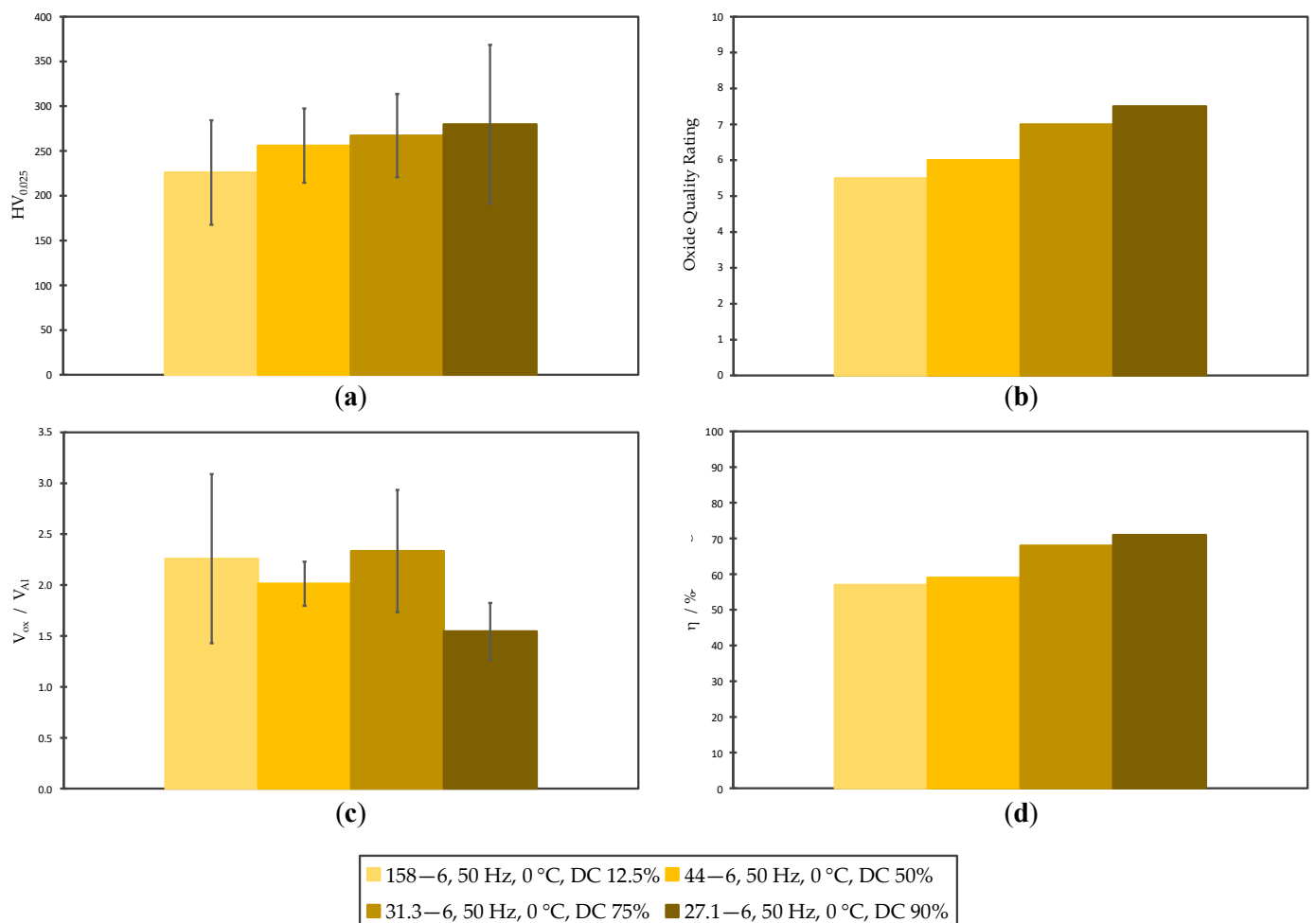


Figure 3. Influence of Duty Cycle on (a) Vickers hardness, (b) Oxide quality rating, (c) Volumetric expansion ratio, and (d) Faradaic efficiency.

Figure 4 depicts the Vickers hardness profiles measured on the anodic oxide cross-section at increasing distances from the metal/oxide interface. Regarding DC procedures, the Vickers hardness profiles of GC and L-PBF samples are similar, Figure 4a. The highest $HV_{0.025}$ values characterize the GC samples, even though, as already mentioned, the $HV_{0.025}$ measurements on GC samples were carried out far away from defects. Low $HV_{0.025}$ standard deviation values characterize the Vickers hardness profiles of the L-PBF samples anodized using DC procedures. This confirms the tribological properties homogeneity in L-PBF samples' anodic oxides. As the distance increases, the samples anodized using the DC procedures show a growing trend, Figure 4a. Conversely, the samples anodized using the PDC procedures exhibit a downward trend due to the action of the sulfuric acid, Figure 4b. This means the PDC procedures allow the defect number at the metal/oxide interface to minimize, hence improving the interfacial compactness of anodic oxide.

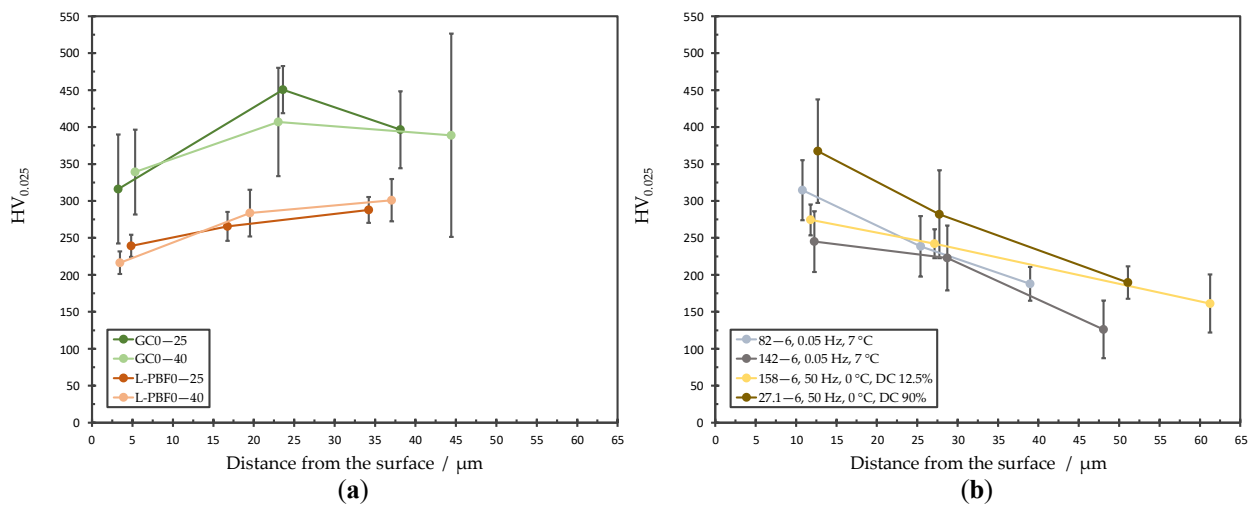


Figure 4. Vickers hardness as a function of the distance from the surface for samples anodized in (a) Direct Current and (b) Pulsed Direct Current (some selected samples to represent the different combinations of electrical parameters applied).

Figure 5 presents the E vs. i potentiodynamic polarization curves (semi-log plot) for the non-anodized and anodized samples.

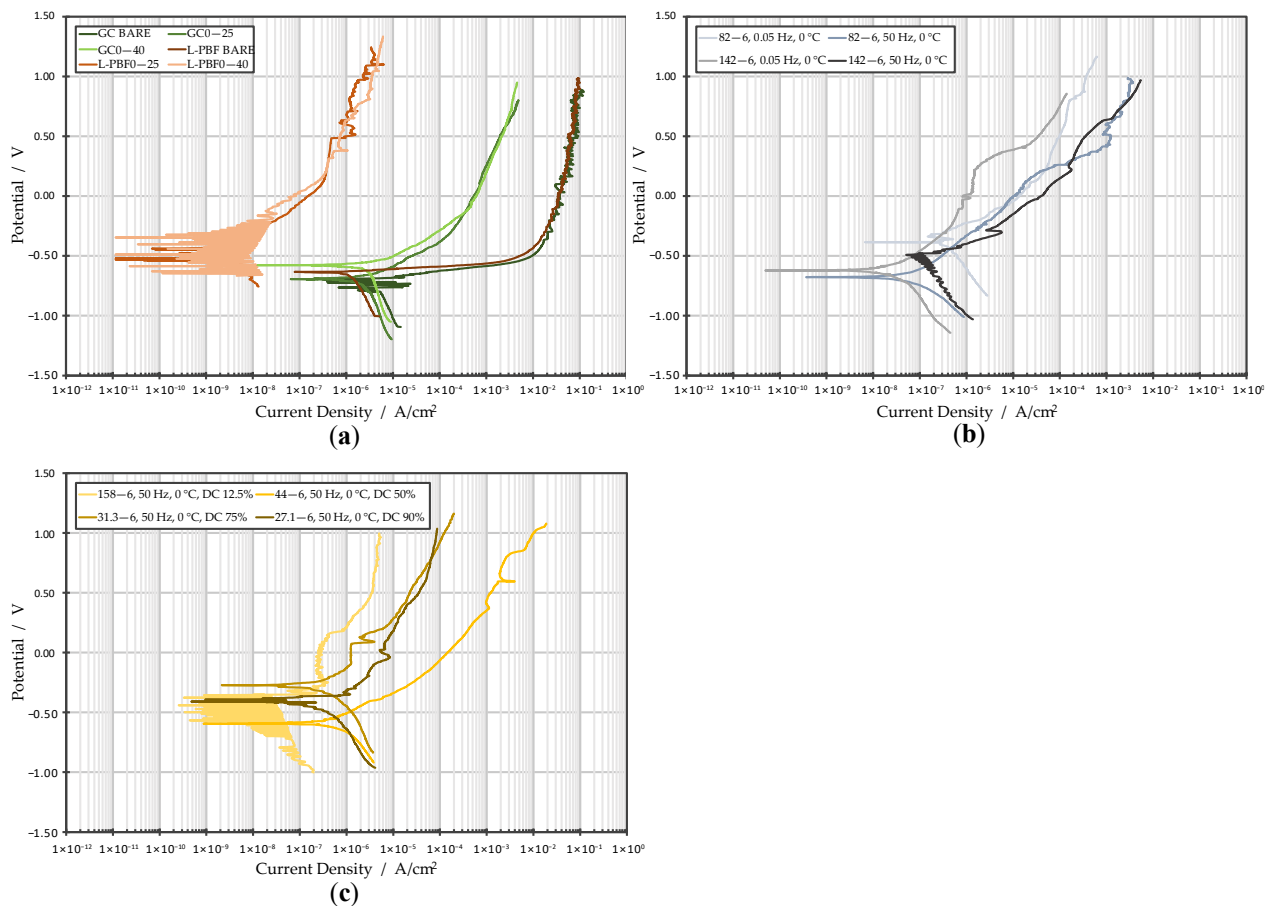


Figure 5. E vs. i potentiodynamic polarization curves (semi-log plot) for samples anodized with (a) Direct Current, (b) Pulsed Direct Current with a 25% of Duty Cycle, and (c) Pulsed Direct Current with a Duty Cycle equal to 12.5–50–75–90%.

The anodic branches of the curves of the non-anodized samples (GC BARE and L-PBF BARE, Figure 5a) rise with a very high slope from the equilibrium potential to the point that it is not possible to identify a “passive region” and a pitting potential. In this case, to better highlight the differences in terms of corrosion resistance, the Tafel analysis was performed in order to obtain the values of corrosion potential (E_{corr}) and corrosion current density (i_{corr}). These values can be used to give an indication of the free-corrosion behavior of Al-Si alloys and can be used to compare the corrosion resistance of alloys produced with GC and L-PBF technology [38,39]; specifically, i_{corr} allows prediction of the corrosion rate of those alloys when exposed to free-corrosion. The results of Tafel analysis for the non-anodized and anodized samples are presented in Table 4.

Table 4. Results obtained through the Tafel analysis.

Sample	E_{corr} (V) vs. SSCE	i_{corr} (A/cm ²)
GC BARE	−0.691	1.08×10^{-5}
GC0—25	−0.693	8.41×10^{-7}
GC0—40	−0.581	1.20×10^{-6}
L-PBF BARE	−0.633	2.76×10^{-6}
L-PBF0—25	−0.535	1.02×10^{-9}
L-PBF0—40	−0.492	8.01×10^{-9}
82—6, 0.05 Hz, 0 °C	−0.336	2.00×10^{-7}
82—6, 50 Hz, 0 °C	−0.686	3.08×10^{-8}
142—6, 0.05 Hz, 0 °C	−0.619	9.45×10^{-9}
142—6, 50 Hz, 0 °C	−0.497	1.29×10^{-7}
158—6, 50 Hz, 0 °C, DC 12.5%	−0.365	2.49×10^{-8}
44—6, 50 Hz, 0 °C, DC 50%	−0.591	2.64×10^{-7}
31.3—6, 50 Hz, 0 °C, DC 75%	−0.283	8.94×10^{-8}
27.1—6, 50 Hz, 0 °C, DC 90%	−0.388	9.59×10^{-8}

Compared to “GC BARE”, the “L-PBF BARE” specimen is characterized by a corrosion current density value of one order of magnitude lower. It is well known from the literature that the presence of micro-scale eutectic silicon particles results in the formation of macro-galvanic couples where the silicon acts as a cathode [38,39]; in contrast, the ultrafine eutectic silicon particles of the L-PBF samples (see Figure 1d) act as micro-cathodes on the surface of the alloy and allow the formation of numerous micro-galvanic couples, which enhance the formation of a compact Al₂O₃ film [38,39]. Therefore, the superfine network of Si particles distributed in the aluminum matrix allows reduction of the cathode/anode surface area ratio (the silicon distribution is very homogeneous, avoiding the formation of strong localized galvanic cells) and, as a consequence, it improves the corrosion resistance behavior of the alloy [38–40].

The polarization curves obtained on the anodized samples (Figure 5a–c) have a very different trend compared to those of the non-anodized samples; the anodic branch shows a slight current increase as the applied polarization raises, and in general lower current values are reached. This behavior can be ascribed to the protection offered by the anodic oxide layer created on the surface, which hinders the reaching of the metal/oxide interface by the electrolyte; it should be emphasized that the samples were placed in contact with the electrolyte for 5 min (during the acquisition of the OCP) before the polarization curves were acquired, to allow the entry of the solution through the defects and porosity of the oxide; therefore, the current density values obtained can be related to the different permeability of the oxide to the electrolyte, derived from the more or less marked presence of defects or open pores [41,42]. Furthermore, considering that the specimens were tested exactly 5 days after the formation of the anodic oxide to allow the natural (i.e., in air, by means of atmospheric humidity) sealing process to take place in the same way as on all the coatings

obtained, the current density of the anodic branch can be related to the presence of defects in the oxide (both in the porous and in the barrier layer) [41,42].

To compare the different levels of protection (and therefore of defects) of the different anodic oxides obtained, the corrosion current density (i_{corr}) of each sample was calculated through Tafel analysis (Table 4), according to the literature [41,42]. The “GC0—25” and “GC0—40” specimens are marked by corrosion current density values of one order of magnitude lower than the “GC BARE” one. Similarly, the “L-PBF0—25” and “L-PBF0—40” specimens are characterized by corrosion current density values of three orders of magnitude lower than the “L-PBF BARE” one. This means that the hard anodizing treatments using DC procedures strongly improves the corrosion resistance behavior (as expected and described above), but the improvement is higher in the case of L-PBF samples. As a consequence of their worse microstructural inhomogeneity, the “GC0—25” and “GC0—40” specimens are marked by corrosion current density values of at least two orders of magnitude higher than the “L-PBF0—25” and “L-PBF0—40” ones; this means that, in the presence of microstructural defects on the surface of the alloy (i.e., micro-scale eutectic silicon particles), even the microstructure of the anodic oxide will be very defective (as already see in Figure 2). In relation to DC procedures, the application of PDC procedures leads to a decrease in corrosion resistance. Nevertheless, it is important to observe that the corrosion current density of all the samples obtained with the PDC procedure is still better (i.e., lower) than those obtained on GC samples and is at least one order of magnitude lower than the “L-PBF BARE” value. This means that the PDC anodizing procedures still ensure a good protection against corrosion, but this is less effective than that obtainable with the DC procedure. To better investigate the reasons behind this decrease in corrosion resistance in the anodic coating obtained with the PDC procedure, some impedance spectra were acquired. From the literature, it is well known that through the analysis of the impedance spectra it is possible to investigate in depth the protection offered by protective coatings [43,44] and, in particular, considering anodic oxides grown on the aluminum alloys, it is possible to evaluate the protection offered by the different oxide layers (i.e., barrier layer and porous layer) [45,46].

The impedance spectra were acquired on the non-anodized “L-PBF BARE” sample, on the L-PBF samples anodized with the DC procedure at temperature 0 °C and on the L-PBF samples anodized with all PCD procedures at temperature 0 °C. All the acquired spectra show a semicircle in the first quadrant of the Nyquist diagrams, but as expected the impedance modules obtained for anodized samples are higher than that of the “L-PBF BARE” sample. For the fitting of the spectrum obtained on the non-anodized “L-PBF BARE” sample, a simple R(QR) equivalent circuit was used, obtaining good results; for all the anodized samples a more complex equivalent circuit was used, following a model reported in the literature that considers two additional (QR) meshes to represent the barrier layer and the porous layer obtained after anodization [45]. Figure 6 shows two examples of fitting of the Nyquist plots obtained with the EIS experiments, using an R(QR) equivalent circuit for the “L-PBF BARE” specimen and an R(QR)(QR)(QR) equivalent circuit for the “31.3—6, 50 Hz, 0 °C, DC 75%” specimen, where an excellent coherence between experimental data and calculated data is observable.

The results of fitting of the Nyquist plot using the R(QR) equivalent electrical circuit for the non-anodized L-PBF sample are listed in Table 5; R_{Ω} is the electrolyte solution resistance, R is the charge transfer resistance, and $Q-Y_0$ and $Q-n$ are the characteristic parameters of the Constant Phase Element associated to the electric double-layer at the aluminum/electrolyte interface.

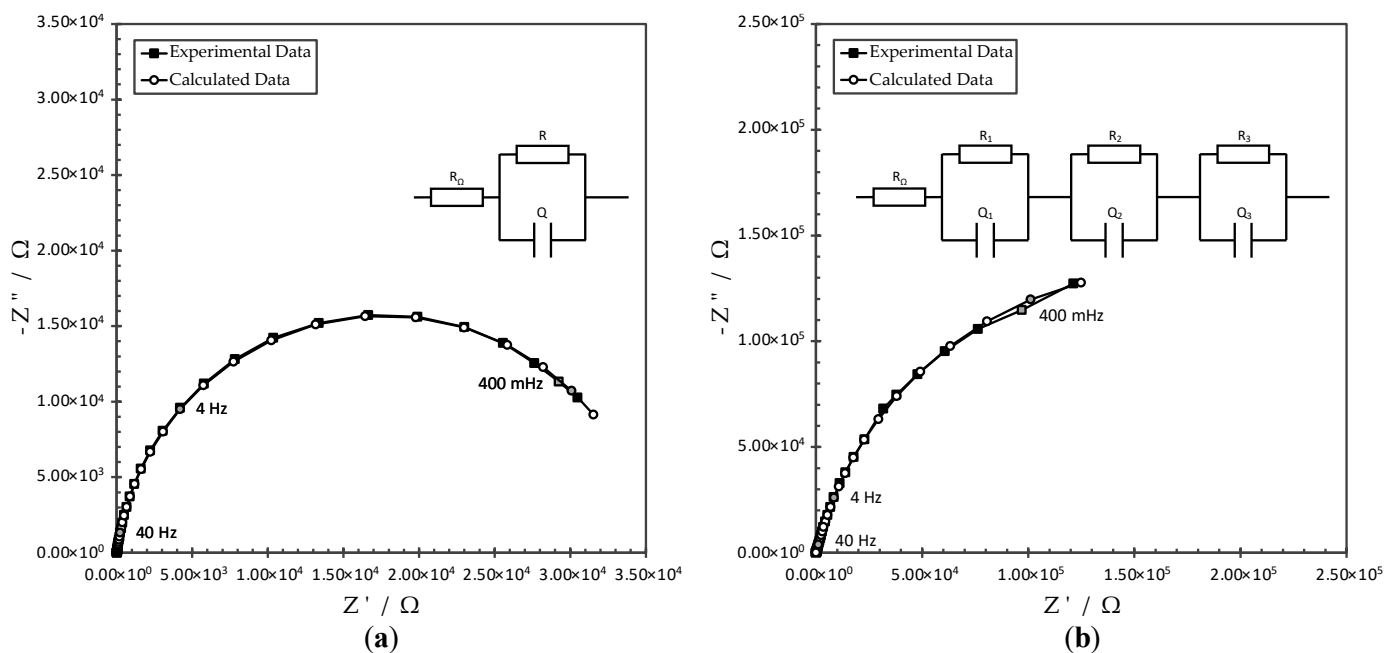


Figure 6. Examples of fitting of the Nyquist plots using (a) R(QR) equivalent electrical circuit for “L-PBF BARE” specimen and (b) R(QR)(QR)(QR) equivalent electrical circuit for “31.3—6, 50 Hz, 0 °C, DC 75%” specimen. In the upper right-hand corners, R_{Ω} is the electrolyte solution resistance, R and R_1 are the charge transfer resistances, R_2 is the porous layer resistance, and R_3 is the barrier layer resistance.

Table 5. Results of interpolation of the Nyquist plot using R(QR) equivalent electrical circuit for “L-PBF BARE” specimen. R_{Ω} is the electrolyte solution resistance and R is the charge transfer resistance.

Sample	R_{Ω}	$Q-Y_0$	$Q-n$	R
	(ohm)	(S · sec ⁿ)	(—)	(ohm)
L-PBF BARE	2.59×10^1	4.54×10^{-6}	9.24×10^{-1}	3.54×10^4

The results of fitting of the Nyquist plots using the R(QR)(QR)(QR) equivalent electrical circuit for the anodized L-PBF samples are reported in Table 6. R_{Ω} is the electrolyte solution resistance; R_1 is the charge transfer resistance across the aluminum/barrier layer oxide interface; R_2 is the porous layer resistance; R_3 is the barrier layer resistance; and Q_1-Y_0 , Q_1-n , Q_2-Y_0 , Q_2-n , Q_3-Y_0 , and Q_3-n are the characteristic parameters of the Constant Phase Elements associated with each of the three (QR) meshes of the equivalent circuit (Q_1 for the aluminum/barrier layer oxide interface, Q_2 for the porous layer, and Q_3 for the barrier layer) [45].

As reported in the literature [45,46], usually the barrier layer contributes more in determining the total impedance of anodized samples, so the barrier layer takes the leading role in the corrosion protection obtained with anodizing. Considering the fitting results reported in Table 6, even in our case the most interesting parameter appears to be R_3 , i.e., the barrier layer resistance; R_3 is the higher resistance value obtained for each sample, so it is the most important parameter to consider when we evaluate the corrosion resistance improvement obtained with anodizing (R_1 and R_2 are negligible when compared to R_3). Moreover, our data come from anodized samples subjected to a simple 5-days natural sealing (i.e., sealing in air, by means of atmospheric humidity) so our R_2 values (resistance of porous layer) are even lower compared to the typical values obtained after chemical-sealing or hot-water sealing [45], making the contribution of the porous layer in determining the whole corrosion resistance of the sample even less relevant. We can assume that the higher the R_3 value, the lower the number of defects (i.e., paths for the passage of electrolyte)

on the barrier layer and, accordingly, the higher the corrosion resistance of the coating. Comparing the R_3 values of the samples anodized using the DC procedures (“L-PBF0—25” and “L-PBF0—40”) with those of the samples anodized using the PDC procedures we can see a slight decrease in the barrier-layer resistance for some of the samples obtained using PDC. This result is in agreement with the data obtained previously (Tafel analysis) and allows us to state that the slight decrease in corrosion resistance observed for some PDC procedures mainly derives from an imperfect growth of the barrier layer. In terms of this, it is worth noting that the “158—6, 50 Hz, 0 °C, DC 12.5%” specimen, obtained with the lower DC% (and thus the higher I_{on} value) has one of the higher R_3 value, specifically, two order of magnitude higher compared to the values obtained for samples anodized with higher DC% (“44—6, 50 Hz, 0 °C, DC 50%”, “31.3—6, 50 Hz, 0 °C, DC 75%”, and “27.1—6, 50 Hz, 0 °C, DC 90%” ones). We have previously seen that under these conditions (low DC% and high I_{on} values) we have silicon oxidation, but a bad quality of the whole oxide grown (i.e., low hardness, high volumetric expansion ration, more defects). Considering all these results, it appears that it is possible to improve the quality of the barrier layer operating with extremely intense pulses (high I_{on}), probably due to the silicon oxidation, which allows for obtaining a compact and homogeneous barrier layer (without defects that act as paths for the electrolyte). However, during the growth of the porous layer, these conditions lead to a greater localization of the electric field, with an increase in parasitic reactions, micro-voids, and defects in the microstructure.

Table 6. Results of interpolation of the Nyquist plots using R(QR)(QR)(QR) equivalent electrical circuit for the anodized L-PBF samples. R_{Ω} is the electrolyte solution resistance, R_1 is the charge transfer resistance, R_2 is the porous layer resistance, and R_3 is the barrier layer resistance.

Sample	R_{Ω} (ohm)	Q_1-Y_0 (S · sec ⁿ)	Q_1-n (—)	R_1 (ohm)	Q_2-Y_0 (S · sec ⁿ)	Q_2-n (—)	R_2 (ohm)	Q_3-Y_0 (S · sec ⁿ)	Q_3-n (—)	R_3 (ohm)
L-PBF0—25	5.01×10^{-2}	5.37×10^{-7}	8.25×10^{-1}	2.74×10^3	6.79×10^{-9}	1.00×10^0	5.44×10^1	1.28×10^{-6}	7.49×10^{-1}	7.06×10^5
L-PBF0—40	2.40×10^{-2}	5.53×10^{-9}	1.00×10^0	4.70×10^1	9.02×10^{-7}	8.32×10^{-1}	1.24×10^3	1.60×10^{-6}	7.62×10^{-1}	1.65×10^7
82—6, 0.05 Hz, 0 °C	2.75×10^1	3.05×10^{-5}	6.42×10^{-1}	9.30×10^2	4.68×10^{-5}	5.45×10^{-1}	1.32×10^2	3.15×10^{-6}	9.18×10^{-1}	2.65×10^5
82—6, 50 Hz, 0 °C	2.81×10^1	2.07×10^{-6}	8.28×10^{-1}	2.63×10^4	8.39×10^{-7}	8.79×10^{-1}	3.21×10^3	2.90×10^{-6}	7.80×10^{-1}	9.92×10^6
142—6, 0.05 Hz, 0 °C	2.47×10^1	3.28×10^{-7}	1.00×10^0	1.86×10^2	1.92×10^{-6}	8.09×10^{-1}	1.78×10^3	1.77×10^{-6}	7.42×10^{-1}	4.33×10^7
142—6, 50 Hz, 0 °C	3.19×10^1	1.87×10^{-5}	6.89×10^{-1}	1.82×10^3	2.28×10^{-6}	8.17×10^{-1}	4.49×10^2	3.29×10^{-6}	9.06×10^{-1}	8.47×10^5
158—6, 50 Hz, 0 °C, DC 12.5%	2.89×10^1	3.07×10^{-6}	7.34×10^{-1}	3.32×10^3	2.39×10^{-15}	4.04×10^{-1}	8.58×10^{-1}	3.61×10^{-6}	8.96×10^{-1}	3.27×10^7
44—6, 50 Hz, 0 °C, DC 50%	2.17×10^0	1.63×10^{-8}	9.30×10^{-1}	3.61×10^1	8.16×10^{-6}	7.27×10^{-1}	4.95×10^4	2.48×10^{-6}	1.00×10^0	1.42×10^5
31.3—6, 50 Hz, 0 °C, DC 75%	1.46×10^{-2}	3.06×10^{-5}	7.36×10^{-1}	2.43×10^2	2.42×10^{-8}	9.20×10^{-1}	4.36×10^1	2.29×10^{-6}	8.55×10^{-1}	3.36×10^5
27.1—6, 50 Hz, 0 °C, DC 90%	9.90×10^{-1}	9.50×10^{-20}	6.12×10^{-1}	3.78×10^1	2.30×10^{-5}	6.42×10^{-1}	1.15×10^3	1.75×10^{-6}	9.07×10^{-1}	3.35×10^5

4. Conclusions

The AlSi10Mg samples, fabricated by GC and L-PBF, were hard anodized in a traditional sulfuric bath by adopting several DC and PDC procedures. Different electrical parameter combinations were tested in order to reach the optimal compromise between the corrosion resistance and mechanical properties (i.e., hardness) of the oxide. The subsequent characterization analyses led to the following conclusions:

1. Compared to the as-produced GC sample, the as-produced L-PBF sample presented a better corrosion resistance behavior related to the superfine network of Si particles distributed in its anodic oxide layer.

2. Unlike the anodized GC samples, the anodized L-PBF samples are marked by homogeneous anodic oxide layers. The uniform distribution of very fine Si particles in the L-PBF samples avoids the formation of punctual defects, e.g., conical asperities, which are responsible for the inhomogeneous anodic oxide growth.
3. Neither the DC procedures nor the PDC procedures completely resolved the critical feature of the anodized L-PBF samples, i.e., the low hardness of the oxide. Operating in DC with a high current level allows the hardness of the oxide to increase due to silicon oxidation, but it compromises the quality of the oxide in terms of defects and volumetric expansion ratio (not allowing to reach very high hardness values). On the other hand, operating in PDC, in particular, by increasing the DC% and decreasing the I_{on} value, the microstructural quality of the oxide increases (limited porosity, no defects) but the amount of oxidized silicon decreases. Unfortunately, none of the electrical parameter combinations applied allowed the two effects that lead to an increase in hardness to be simultaneously obtain.
4. The higher corrosion resistance was obtained using the DC procedures on L-PBF samples. The PDC procedures leads in general to a slightly lower corrosion resistance, ascribed to an imperfect growth of the barrier layer; the DC% strongly affect this phenomenon, so lower DC% (which correspond to higher current values during the time-on in our procedures) allows the best results in terms of corrosion resistance to be obtained.
5. Considering microstructure, hardness, and corrosion resistance, the best compromise obtained among the investigated DC and PDC procedures is represented by the “27.1—6, 50 Hz, 0 °C, DC 90%” cycle. Using this PDC procedure, it was possible to obtain an anodic oxide with the highest $HV_{0.025}$ and the lowest V_{ox}/V_{Al} values without compromising the oxide quality and the corrosion resistance behavior.

The results obtained confirm that PDC procedures are very interesting when applied to hard anodizing of L-PBF AlSi10Mg alloy because they offer specific combinations of electrical parameters that are able to maximize the hardness, corrosion resistance, or microstructural quality of the anodic oxide produced. The limitation of the technique is that it does not allow all these aspects of the oxide to be maximized simultaneously (but very good compromises can still be obtained) and that, in terms of oxide hardness, the maximum values obtained do not reach those of anodized aluminum wrought alloys.

Author Contributions: Conceptualization, M.B., R.G., A.P. and P.V.; methodology, M.B., E.D. and R.G.; validation, M.B., E.D. and R.G.; formal analysis, M.B., E.D. and M.T.; investigation, M.B., E.D., R.G., A.P. and M.T.; resources, R.G., A.P. and P.V.; data curation, M.B., E.D. and R.G.; writing—original draft preparation, E.D. and M.T.; writing—review and editing, E.D., R.G. and M.T.; visualization, E.D., R.G., A.P., M.T. and P.V.; supervision, R.G., A.P. and P.V.; project administration R.G.; funding acquisition, R.G. and A.P. All authors have read and agreed to the published version of the manuscript.

Funding: Financed by the European Union—NextGenerationEU (National Sustainable Mobility Center CN00000023, Italian Ministry of University and Research Decree n. 1033—17/06/2022, Spoke 11—Innovative Materials & Lightweighting). The opinions expressed are those of the authors only and should not be considered as representative of the European Union or the European Commission’s official position. Neither the European Union nor the European Commission can be held responsible for them.

Institutional Review Board Statement: Not applicable.

Informed Consent Statement: Not applicable.

Data Availability Statement: The research data are provided on request.

Conflicts of Interest: The authors declare no conflict of interest.

References

1. Stevenson, M.F., Jr. Anodizing. In *Surface Engineering*; Cotell, C.M., Sprague, J.A., Smidt, F.A., Jr., Eds.; ASM International: Novelty, OH, USA, 1994; Volume 5, ISBN 978-1-62708-170-2.
2. Zhu, B.; Fedel, M.; Andersson, N.-E.; Leisner, P.; Deflorian, F.; Zanella, C. Effect of Si Content and Morphology on Corrosion Resistance of Anodized Cast Al-Si Alloys. *J. Electrochem. Soc.* **2017**, *164*, C435–C441. [[CrossRef](#)]
3. Zhu, B.; Seifeddine, S.; Persson, P.O.Å.; Jarfors, A.E.W.; Leisner, P.; Zanella, C. A Study of Formation and Growth of the Anodised Surface Layer on Cast Al-Si Alloys Based on Different Analytical Techniques. *Mater. Des.* **2016**, *101*, 254–262. [[CrossRef](#)]
4. Fratila-Apachitei, L.E.; Terry, H.; Skeldon, P.; Thompson, G.E.; Duszczyc, J.; Katgerman, L. Influence of Substrate Microstructure on the Growth of Anodic Oxide Layers. *Electrochim. Acta* **2004**, *49*, 1127–1140. [[CrossRef](#)]
5. Fratila-Apachitei, L.E.; Tichelaar, F.D.; Thompson, G.E.; Terry, H.; Skeldon, P.; Duszczyc, J.; Katgerman, L. A Transmission Electron Microscopy Study of Hard Anodic Oxide Layers on AlSi(Cu) Alloys. *Electrochim. Acta* **2004**, *49*, 3169–3177. [[CrossRef](#)]
6. Scampone, G.; Timelli, G. Anodizing Al-Si Foundry Alloys: A Critical Review. *Adv. Eng. Mater.* **2022**, *24*, 2101480. [[CrossRef](#)]
7. Zhu, B.; Zanella, C. Hardness and Corrosion Behaviour of Anodised Al-Si Produced by Rheocasting. *Mater. Des.* **2019**, *173*, 107764. [[CrossRef](#)]
8. Riddar, F.; Hogmark, S.; Rudolphi, Å.K. Comparison of Anodised Aluminium Surfaces from Four Fabrication Methods. *J. Mater. Process. Technol.* **2012**, *212*, 2272–2281. [[CrossRef](#)]
9. Wu, J.; Wang, X.Q.; Wang, W.; Attallah, M.M.; Loretto, M.H. Microstructure and Strength of Selectively Laser Melted AlSi10Mg. *Acta Mater.* **2016**, *117*, 311–320. [[CrossRef](#)]
10. Lam, L.P.; Zhang, D.Q.; Liu, Z.H.; Chua, C.K. Phase Analysis and Microstructure Characterisation of AlSi10Mg Parts Produced by Selective Laser Melting. *Virtual Phys. Prototyp.* **2015**, *10*, 207–215. [[CrossRef](#)]
11. Aboulkhair, N.T.; Simonelli, M.; Parry, L.; Ashcroft, I.; Tuck, C.; Hague, R. 3D Printing of Aluminium Alloys: Additive Manufacturing of Aluminium Alloys Using Selective Laser Melting. *Prog. Mater. Sci.* **2019**, *106*, 100578. [[CrossRef](#)]
12. Rubben, T.; Revilla, R.I.; De Graeve, I. Effect of Heat Treatments on the Anodizing Behavior of Additive Manufactured AlSi10Mg. *J. Electrochem. Soc.* **2019**, *166*, C42–C48. [[CrossRef](#)]
13. Revilla, R.I.; Rojas, Y.; De Graeve, I. On the Impact of Si Content and Porosity Artifacts on the Anodizing Behavior of Additive Manufactured Al-Si Alloys. *J. Electrochem. Soc.* **2019**, *166*, C530–C537. [[CrossRef](#)]
14. Revilla, R.I.; Terry, H.; De Graeve, I. Role of Si in the Anodizing Behavior of Al-Si Alloys: Additive Manufactured and Cast Al-Si10-Mg. *J. Electrochem. Soc.* **2018**, *165*, C532–C541. [[CrossRef](#)]
15. Revilla, R.I.; Verkens, D.; Couturiaux, G.; Malet, L.; Thijs, L.; Godet, S.; De Graeve, I. Galvanostatic Anodizing of Additive Manufactured Al-Si10-Mg Alloy. *J. Electrochem. Soc.* **2017**, *164*, C1027–C1034. [[CrossRef](#)]
16. Mohitfar, S.H.; Mahdavi, S.; Etmannfar, M.; Khalil-Allafi, J. Characteristics and Tribological Behavior of the Hard Anodized 6061-T6 Al Alloy. *J. Alloys Compd.* **2020**, *842*, 155988. [[CrossRef](#)]
17. Bononi, M.; Giovanardi, R. Hard Anodizing of AA2011-T3 Al-Cu-Pb-Bi Free-Cutting Alloy: Improvement of the Process Parameters. *Corros. Sci.* **2018**, *141*, 63–71. [[CrossRef](#)]
18. Mukhopadhyay, A.K.; Sharma, A.K. Influence of Fe-Bearing Particles and Nature of Electrolyte on the Hard Anodizing Behaviour of AA 7075 Extrusion Products. *Surf. Coat. Technol.* **1997**, *92*, 212–220. [[CrossRef](#)]
19. Caliar, D.; Timelli, G.; Salata, T.; Cavagnini, G.; Maestri, S.; Manfredini, A. Influence of Microstructure and Surface Finishing on the Hard Anodizing of Diecast Al-Si-Cu Alloys. *Metall. Ital.* **2019**, *111*, 23–31.
20. Konieczny, J.; Labisz, K.; Polok-Rubini, M.; Włodarczyk-Fligier, A. Influence of Aluminium Alloy Anodizing and Casting Methods on Structure and Functional Properties. *Arch. Metall. Mater.* **2016**, *61*, 1337–1342. [[CrossRef](#)]
21. Bononi, M.; Conte, M.; Giovanardi, R.; Bozza, A. Hard Anodizing of AA2099-T8 Aluminum-lithium-copper Alloy: Influence of Electric Cycle, Electrolytic Bath Composition and Temperature. *Surf. Coat. Technol.* **2017**, *325*, 627–635. [[CrossRef](#)]
22. Bononi, M.; Giovanardi, R.; Bozza, A. Pulsed Current Hard Anodizing of Heat Treated Aluminum Alloys: Frequency and Current Amplitude Influence. *Surf. Coat. Technol.* **2016**, *307*, 861–870. [[CrossRef](#)]
23. Bononi, M.; Giovanardi, R.; Bozza, A.; Mattioli, P. Pulsed Current Effect on Hard Anodizing Process of 2024-T3 Aluminium Alloy. *Surf. Coat. Technol.* **2016**, *289*, 110–117. [[CrossRef](#)]
24. Chiang, M.-H.; Yeh, C.-C.; Lee, C.-L. Improvement in the Abrasive Wear Resistance of an Aluminum Alloy Casting for a Continuously-Variable Transmission Using Heat Treatment and Pulsed Anodizing. *Wear* **2020**, *442–443*, 203137. [[CrossRef](#)]
25. Girelli, L.; Tocci, M.; Conte, M.; Giovanardi, R.; Veronesi, P.; Gelfi, M.; Pola, A. Effect of the T6 Heat Treatment on Corrosion Behavior of Additive Manufactured and Gravity Cast AlSi10Mg Alloy. *Mater. Corros.* **2019**, *70*, 1808–1816. [[CrossRef](#)]
26. Bozza, A.; Giovanardi, R.; Manfredini, T.; Mattioli, P. Pulsed Current Effect on Hard Anodizing Process of 7075-T6 Aluminium Alloy. *Surf. Coat. Technol.* **2015**, *270*, 139–144. [[CrossRef](#)]
27. Aperador, W.; Delgado, A.; Bautista, J. Improved Corrosion Protection Properties in Anodic Films Type Porous on 2024 T3 Aluminium Alloys Obtained by Pulse Reverse Plating. *Int. J. Electrochem. Sci.* **2013**, *8*, 9607–9617.
28. Juhl, A.D. Why It Makes Sense to Upgrade to Pulse Anodizing. *Met. Finish.* **2009**, *107*, 24–27. [[CrossRef](#)]
29. Qian, J.; Wang, C.; Li, D.; Guo, B.; Song, G. Formation Mechanism of Pulse Current Anodized Film on AZ91D Mg Alloy. *Trans. Nonferrous Met. Soc. China* **2008**, *18*, 19–23. [[CrossRef](#)]
30. Kanagaraj, D.; Raj, V.; Vincent, S.; Iyer, S.V. Effect of Pulse Frequency on Pulse Anodising of AA 1100 Aluminium Alloy in Sulphamic Acid. *Bull. Electrochem.* **2001**, *17*, 523–526.

31. Kanagaraj, D.; Raj, V.; Vincent, S.; Kumar, B.P.; Kumar, A.S.; Iyer, S.V.K. Pulse Anodizing of AA1100 Aluminium Alloy in Oxalic Acid Electrolyte. *Bull. Electrochem.* **2001**, *17*, 285–288.
32. Poinern, G.E.J.; Ali, N.; Fawcett, D. Progress in Nano-Engineered Anodic Aluminum Oxide Membrane Development. *Materials* **2011**, *4*, 487–526. [[CrossRef](#)]
33. Arurault, L. Pilling–Bedworth Ratio of Thick Anodic Aluminium Porous Films Prepared at High Voltages in H₂ SO₄ Based Electrolyte. *Trans. IMF* **2008**, *86*, 51–54. [[CrossRef](#)]
34. Hamann, C.H.; Hamnett, A.; Vielstich, W. *Electrochemistry*; Wiley: New York, NY, USA, 2007; ISBN 978-3-527-31069-2.
35. ASTM International. *ASTM G3—Standard Practice for Conventions Applicable to Electrochemical Measurements in Corrosion Testing*; ASTM International: West Conshohocken, PA, USA, 2014.
36. ASTM International. *ASTM G5—Standard Reference Test Method for Making Potentiodynamic Anodic Polarization Measurements*; ASTM International: West Conshohocken, PA, USA, 2014.
37. Runge, J.M. *The Metallurgy of Anodizing Aluminum*; Springer International Publishing: Cham, Switzerland, 2018; ISBN 978-3-319-72175-0.
38. Yang, Y.; Chen, Y.; Zhang, J.; Gu, X.; Qin, P.; Dai, N.; Li, X.; Kruth, J.-P.; Zhang, L.-C. Improved Corrosion Behavior of Ultrafine-Grained Eutectic Al-12Si Alloy Produced by Selective Laser Melting. *Mater. Des.* **2018**, *146*, 239–248. [[CrossRef](#)]
39. Leon, A.; Shirizly, A.; Aghion, E. Corrosion Behavior of AlSi10Mg Alloy Produced by Additive Manufacturing (AM) vs. Its Counterpart Gravity Cast Alloy. *Metals* **2016**, *6*, 148. [[CrossRef](#)]
40. Wang, X.; Nie, M.; Wang, C.T.; Wang, S.C.; Gao, N. Microhardness and Corrosion Properties of Hypoeutectic Al–7Si Alloy Processed by High-Pressure Torsion. *Mater. Des.* **2015**, *83*, 193–202. [[CrossRef](#)]
41. Li, J.; Wei, H.; Zhao, K.; Wang, M.; Chen, D.; Chen, M. Effect of Anodizing Temperature and Organic Acid Addition on the Structure and Corrosion Resistance of Anodic Aluminum Oxide Films. *Thin Solid Film.* **2020**, *713*, 138359. [[CrossRef](#)]
42. He, C.; Lou, D.; Wang, J.; Cai, Q. Corrosion Protection and Formation Mechanism of Anodic Coating on SiCp/Al Metal Matrix Composite. *Thin Solid Film.* **2011**, *519*, 4759–4764. [[CrossRef](#)]
43. Zhang, Y.; Shen, X. Facile Fabrication of Robust Superhydrophobic Coating for Enhanced Corrosion Protection on AZ91 Magnesium Alloy by Electroless Ni-B/GO Plating. *Surf. Coat. Technol.* **2023**, *455*, 129213. [[CrossRef](#)]
44. Qin, J.; Shi, X.; Li, H.; Zhao, R.; Li, G.; Zhang, S.; Ding, L.; Cui, X.; Zhao, Y.; Zhang, R. Performance and Failure Process of Green Recycling Solutions for Preparing High Degradation Resistance Coating on Biomedical Magnesium Alloys. *Green Chem.* **2022**, *24*, 8113–8130. [[CrossRef](#)]
45. Hakimizad, A.; Raeissi, K.; Ashrafizadeh, F. A Comparative Study of Corrosion Performance of Sealed Anodized Layers of Conventionally Colored and Interference-Colored Aluminium. *Surf. Coat. Technol.* **2012**, *206*, 4628–4633. [[CrossRef](#)]
46. Brevnov, D.A.; Rama Rao, G.V.; López, G.P.; Atanassov, P.B. Dynamics and Temperature Dependence of Etching Processes of Porous and Barrier Aluminum Oxide Layers. *Electrochim. Acta* **2004**, *49*, 2487–2494. [[CrossRef](#)]

Disclaimer/Publisher’s Note: The statements, opinions and data contained in all publications are solely those of the individual author(s) and contributor(s) and not of MDPI and/or the editor(s). MDPI and/or the editor(s) disclaim responsibility for any injury to people or property resulting from any ideas, methods, instructions or products referred to in the content.